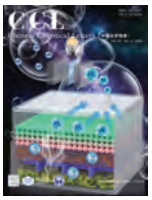
Chinese Chemical Letters 37 (2026) 111199

Contents lists available at ScienceDirect

Chinese Chemical Letters

journal homepage: www.elsevier.com/locate/cclet



NIR-enhanced oxidase-like activity of manganese dioxide nanoparticles for combating subcutaneous methicillin-resistant *Staphylococcus aureus* infections

Jing Zhao [a], Tian Huang [a], Dongyang Zhang [d], Jianliang Shen [b,c,*], Jintao Wang [a,*]

[a] School of Pharmacy, Jiangxi Science & Technology Normal University, Nanchang 330013, China
[b] National Engineering Research Center of Ophthalmology and Optometry, Eye Hospital, Wenzhou Medical University, Wenzhou 325027, China
[c] Zhejiang Engineering Research Center for Tissue Repair Materials, Wenzhou Institute, University of Chinese Academy of Sciences, Wenzhou 325001, China
[d] Guangzhou Municipal and Guangdong Provincial Key Laboratory of Molecular Target & Clinical Pharmacology, the NMPA and State Key Laboratory of Respiratory Disease, the Fifth Affiliated Hospital and School of Pharmaceutical Sciences, Guangzhou Medical University, Guangzhou 511436, China

ARTICLE INFO

Article history:
Received 23 December 2024
Revised 8 April 2025
Accepted 10 April 2025
Available online 12 April 2025

Keywords:
Manganese oxide
Photothermal therapy
Oxidase-like activity
Anti-biofilm therapy
Anti-infection therapy

ABSTRACT

The inappropriate use of antibiotics has led to the emergence of drug-resistant bacteria and the formation of persistent biofilms, rendering conventional antibiotics ineffective against these infections. To address this challenge, the enzyme-like activity of nanozymes, particularly those with photothermal effects, is being explored. However, the development of nanozymes is hindered by the complex synthesis processes involved and the consumption of reactive oxygen species (ROS) by reducing products in bacteria. This article presents an interesting strategy utilizing near-infrared laser-enhanced oxidase-like (OXD-like) activity of manganese dioxide nanoparticles (MnO_2 NPs) to combat subcutaneous infections caused by methicillin-resistant *Staphylococcus aureus* (MRSA). MnO_2 NPs, characterized by flower-like morphology and broad near-infrared absorption, exhibited favorable OXD-like activity and a stable photothermal effect. Experiments *in vitro* revealed that the combined high thermal effect and the substantial production of ROS effectively targeted MRSA and disrupted biofilm. The efficacy of MnO_2 *in vivo* was validated through the establishment of a subcutaneous abscess model. Additionally, a series of biosafety tests, including routine blood tests and blood biochemistry analyses, confirmed the safety of MnO_2 *in vivo*. Collectively, these findings suggest that combination therapy involving MnO_2 presents a promising therapeutic approach for addressing infections associated with biofilms and drug-resistant bacteria.

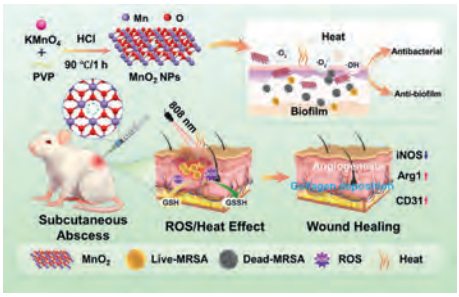
© 2026 Published by Elsevier B.V. on behalf of Chinese Chemical Society and Institute of Materia Medica, Chinese Academy of Medical Sciences.

Drug-resistant bacteria are responsible for numerous illnesses, injuries, and economic losses, with methicillin-resistant *Staphylococcus aureus* (MRSA) being a notable contributor to various infections [1–3]. Furthermore, biofilms, characterized by their strong adhesion and dense structure, exhibit resistance to conventional treatments. Extracellular polymeric substance (EPS) within biofilms acts as barriers during antibiotic therapy, limiting the penetration of antibiotics and hindering drug-bacteria interactions [4–7]. These result in prolonged treatment durations for infections and contribute to the ineffectiveness of antibacterial drugs. Nanozymes have been extensively investigated as alternatives to antibiotics for treating drug-resistant bacterial infections. These nanozymes exploit their remarkable catalytic activity to generate significant amounts of toxic reactive oxygen species (ROS) within the infected microenvironment, which subsequently disrupt bacterial cell membranes and biomolecules, ultimately leading to bacterial death. Liu's team [8] utilized the oxidase (OXD)-like activity of Pd-loaded metallophenolic networks to produce ROS, effectively treating periodontitis. Similarly, Yin's team [9] combined catalase-like, glucose OXD-like, and peroxidase-like activities to implement a "three-in-one" cascade therapy. Nanozymatic materials are typically non-destructive and exhibit minimal toxic side effects [10–12]. However, ROS is inherently unstable and can be readily scavenged by glutathione produced by bacteria, limiting the efficacy of single ROS-based approach [13–15].

The significance of photothermal therapy (PTT) as a promising alternative to traditional antibiotic treatments stems from the use of photosensitisers with optimal photothermal conversion efficiencies. The photothermal conversion in PTT occurs *via* localized heating of the plasma, non-radiative relaxation, or molecular ther-

* Corresponding authors.
E-mail addresses: shenjl@wiucas.ac.cn (J. Shen), jintaochem@163.com (J. Wang).

https://doi.org/10.1016/j.cclet.2025.111199
1001-8417/© 2026 Published by Elsevier B.V. on behalf of Chinese Chemical Society and Institute of Materia Medica, Chinese Academy of Medical Sciences.



Scheme 1. The description of the synthesis of MnO_2 NPs and the efficacy of 808 nm laser irradiation to enhance the enzyme-like activity of MnO_2 on MRSA-infected abscesses *in vivo*.

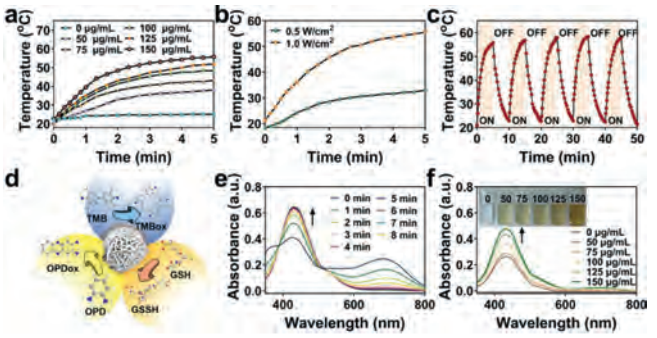


Fig. 1. Photothermal and enzyme-like property of MnO_2. (a) Photothermal heating curves of MnO_2 dispersions at different concentrations under 808 nm laser irradiation (1.0 W/cm^2). (b) Photothermal heating curves of MnO_2 dispersion (150 μg/mL) at different laser power intensities. (c) Photothermal stability (five on/off laser cycles) of MnO_2 dispersion. (d) Schematic diagram of the catalytic action of MnO_2 nanozyme. (e) The OXD-like activity of MnO_2 dispersion using OPD as substrate at various times. (f) The OXD-like activity of MnO_2 dispersion using OPD as substrate at various concentrations.

mal vibrations, effectively absorbing photon energy in the near-infrared (NIR) spectrum and transforming it into heat energy. This process results in the destruction of bacterial DNA and proteins, leading to severe and irreversible effects that achieve effective sterilization [16]. PTT can be categorized into three stages based on the resultant temperature: mild heat (37–42 °C), thermal therapy (42–48 °C), and thermal ablation (>48 °C) [17–19]. Under the high-temperature conditions associated with PTT, biologically active substrates within the biofilm, such as EPS, including polysaccharides and nucleic acids, may be inactivated. Recently, manganese-based nanosystems have gained significant traction in biomedical research due to their tunable physical and morphological characteristics—such as rod-like, spherical, and flower-like forms which can be tailored to meet specific application requirements—as well as their superior biosafety and notable degradability [20–22]. Among these, flower-like MnO_2 stands out for its remarkable properties, including the [MnO_6] octahedral basic structural unit, the presence of oxygen vacancies, and a high specific surface area, which have garnered considerable interest in both catalytic and biotherapeutic applications [23–25]. The oxygen vacancy-defective structure of flower-like MnO_2 enhances its catalytic activity by providing additional active sites [26,27].

In this article, flower-like manganese dioxide nanoparticles (MnO_2 NPs) were synthesized using the optimized aqueous method developed by Huang's team [28]. These flower-like MnO_2 NPs are capable of adsorbing NIR photon energy and converting it into thermal energy. The photothermal effects enhanced the OXD-like activity of MnO_2. By leveraging both photothermal and catalytic properties, MnO_2 NPs demonstrate significant antibacterial and anti-biofilm effects *in vitro*. *In vivo*, they promote collagen deposition and neovascularization, modulate macrophage differentiation, and accelerate wound healing. Consequently, the method proposed in this study for treating subcutaneous MRSA infections—combining OXD-like activity with PTT—represents an effective non-antibiotic therapeutic strategy with broad biomedical application prospects (Scheme 1).

As shown in Fig. S1 (Supporting information), MnO_2 nanoflowers were synthesized using a straightforward and time-efficient aqueous method reported in the literature [28], with the preparation process illustrated in Fig. S1a. The morphology of MnO_2 is depicted in Figs. S1b and c, showing flower-like of uniform size. The high-resolution transmission electron microscopy (HR-TEM) image (Fig. S1d) reveals clear and ordered lattice stripes with a lattice spacing of 0.28 nm, indicative of the nanoflower-like MnO_2 (002) crystal surface. Selected area electron diffraction (SAED) analysis (Fig. S1e) exhibited two diffraction rings, confirming the complete crystallinity of MnO_2. High angle annular dark field-scanning transmission electron microscopy (HAADF-STEM) images (Figs. S1f–i) further illustrated the homogeneous distribution of elemental Mn and O in MnO_2. The X-ray diffraction (XRD) spectra of MnO_2, shown in Fig. S1j, correspond to the standard card MnO_2 PDF #18–0802, with 2θ reflections at 12.3°, 24.6°, 36.8°, and 65.7°, corresponding to diffraction peaks in the (002), (101), (006), and (119) planes. Energy dispersive X-ray spectroscopy (EDS) line-scan results in Fig. S1k identified the presence of Mn and O elements in MnO_2, with no interference from other elements. Dynamic light scattering (DLS) analysis determined the particle size of MnO_2 to be 214.7 ± 0.70 nm and the zeta potential to be −26.6 ± 1.92 mV (Figs. S1l and m). The elemental energy spectrum of MnO_2 was further analyzed using X-ray photoelectron spectroscopy (XPS). The full-spectrum scan presented in Fig. S1n reveals three distinct signal peaks: Mn 2p, O 1s, and C 1s. With C 1s (248.8 eV) as a reference, the signal peaks for Mn, as shown in Fig. S1o, were categorized into Mn^{3+} and Mn^{4+}. The corresponding signals for Mn^{3+} were identified at Mn $2p_{1/2}$ (653.5 eV), while the signal for Mn^{4+} was found at Mn $2p_{1/2}$ (654.8 eV). Due to the existence of defects, MnO_2 is converted from stable d^3 (Mn^{4+}) to unstable d^4 (Mn^{3+}) [29,30]. Additionally, the fine mapping of O 1s (Fig. S1p) can be decomposed into lattice oxygen (Olat) and adsorbed oxygen (Oads), corresponding to binding energies of 529.4 and 531.7 eV, respectively. In Fig. S1q, the electron spin resonance (ESR) detection of MnO_2 reveals a prominent signal peak with $g = 2.003$, further confirming the existence of an oxygen vacancy structure within the MnO_2. Oxygen vacancies create additional active sites for MnO_2, enhancing its ability to produce ROS. Consequently, MnO_2 NPs with oxygen vacancies were successfully synthesized.

Subsequently, the absorbance of MnO_2 was evaluated using an ultraviolet-visible (UV–vis)-NIR spectrophotometer. As illustrated in Fig. S2 (Supporting information), the MnO_2 dispersion demonstrated significant laser absorption in the NIR region (Fig. S2a). Fig. S2b depicts the extinction coefficient of MnO_2, which is $\alpha = 4.681$ L g^{-1} cm^{-1}. MnO_2 possesses a moderate extinction coefficient in comparison to other materials (Table S1 in Supporting information), suggesting its potential application as a photothermal agent (PTA). PTA is capable of absorbing photon energy and converting it into thermal energy. Fig. 1a illustrates the real-time temperature changes of MnO_2 at varying concentrations. With increasing MnO_2 concentration, the temperature rose to 2.9, 16.9, 23.3, 31.2, and 33.2 °C, respectively. Similarly, different laser powers exhibited a comparable trend (Fig. 1b). As shown in Fig. 1c, the photothermal effect of MnO_2 remained stable after five on/off cycles. According to the cooling curves (Figs. S2c and d), the photothermal conversion efficiency (PCE %) of MnO_2 was 33.09 %. Fig. S2e visually demonstrates the heating images of H_2O and MnO_2. Furthermore, MnO_2 ranks highly in PCE among various PTAs (Table S1). These re-

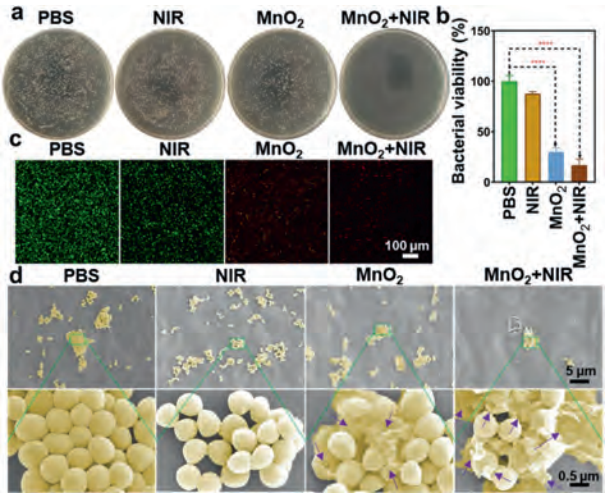


Fig. 2. Antibacterial activity of MnO_2 *in vitro*. (a) Photographs of MRSA colonies incubated with MnO_2 under various conditions, including group 1: PBS, group 2: NIR (808 nm, 1.0 W/cm^2, 5 min), group 3: MnO_2 (150 μg/mL), and group 4: MnO_2 + NIR. (b) Quantitative analysis of bacterial viability of MRSA from Fig. 2a. (c) Representative CLSM images of a live/dead staining assay for MRSA administered different treatments are presented. Scale bar: 100 μm. (d) SEM micrographs were administrated. Scale bar: 5 μm and 0.5 μm. Data are presented as mean ± SD ($n = 3$). $^{****}P < 0.0001$.

sults suggest that MnO_2 exhibits good and stable photothermal activity under NIR irradiation. The enzyme-like activity of MnO_2 was assessed using colorimetric methods, as illustrated in Fig. 1d [31–33]. MnO_2 demonstrated significant OXD-like activity, with optimal performance observed at a pH of 5.6 (Fig. S2f). *o*-Phenylenediamine (OPD) (Figs. 1e and f) and 3,3′,5,5′-tetramethylbenzidine (TMB) (Figs. S2g and h) were employed as ROS detection probes. The results consistently indicated that the OXD-like activity of MnO_2 exhibited both time-dependent and concentration-dependent characteristics. In the inflammatory microenvironment, glutathione (GSH) can neutralize ROS; thus, the depletion of GSH may create a more favorable environment for ROS activity. Notably, MnO_2 effectively depletes GSH (Figs. S2i and j) [34–36]. Based on the photothermal properties of MnO_2, this study incorporated photothermal conditions into the investigation of the OXD-like activity of MnO_2. As illustrated in Fig. S2k, the ROS levels in the NIR (+) group were significantly higher than those in the NIR (−) group, indicating that the OXD-like activity of MnO_2 was enhanced by the photothermal treatment. 5,5-Dimethyl-1-pyrroline-*N*-oxide (DMPO) was employed as an ROS probe, which revealed that the ROS generated by MnO_2 were $^{\bullet}O_2^-$ and $^{\bullet}OH$, as shown in Figs. S3a and b (Supporting information). Furthermore, the catalytic kinetic parameters V_{max} and K_m of MnO_2 were determined through fitting, yielding $K_m = 0.068$ mmol/L and $V_{max} = 8.347 \times 10^{-8}$ mol L^{-1} s^{-1} (Figs. S3c and d in Supporting information). In comparison to the nanozymes detailed in Table S2 (Supporting information), MnO_2 demonstrates a relatively lower K_m and a higher V_{max}, suggesting that MnO_2 exhibits a strong affinity and rapid reaction kinetics as a nanozyme.

Given the exceptional photothermal and OXD-like properties of MnO_2, we anticipate that MnO_2 exhibits ideal antibacterial effects. Initially, the research team evaluated the dark toxicity of MnO_2 against *Escherichia coli* (*E. coli*) and MRSA. As illustrated in Fig. S4a (Supporting information), MnO_2 demonstrated no significant toxicity towards MRSA. Consequently, the relatively resistant MRSA was selected as the experimental strain. The antibacterial results are presented in Figs. 2a and b, where the bacterial survival rate in the MnO_2 + NIR group was recorded at 16.90%, indicating its strongest bactericidal capability compared with other groups. Confocal laser scanning microscope (CLSM) imaging further confirmed the synergistic effect of the photothermal and catalytic activities of MnO_2 (Fig. 2c and Fig. S4b in Supporting information). Scanning electron microscope (SEM) imaging revealed that the bacterial morphology after MnO_2 + NIR treatment exhibited surface damage and content leakage, as indicated by the purple arrows in Fig. 2d. 2′,7′-Dichlorodihydrofluorescein diacetate (DCFH-DA), a fluorescent probe, was employed to observe the ROS signals generated by MnO_2. As shown in Figs. S4c and d (Supporting information), the final treatment group displayed significantly stronger green fluorescence. The *in vitro* antibacterial results of MnO_2 were consistent with the anticipated effects. To address infections caused by biofilms, MnO_2 was introduced during both the formation and maturation stages of these biofilms. In the crystal violet staining experiments for mature biofilms (Figs. S4e and f in Supporting information), the biofilm biomass in the MnO_2 + NIR group was reduced to only 20.30%. Three-dimensional (3D) imaging of biofilms *via* CLSM revealed that the mortality rate in this group reached 95.80% (Figs. S4g and h in Supporting information). For immature biofilms, inhibition is illustrated in Figs. S5a and b (Supporting information), where the crystal violet staining results showed a significant difference between the phosphate buffered saline (PBS) group and the MnO_2 + NIR group. Figs. S5c and d (Supporting information) provide 3D views, as well as frontal and side views of the biofilms, indicating that the MnO_2 + NIR group has a significant inhibitory effect on biofilms. Overall, the photothermal synergistic OXD-like activity of MnO_2 is effective in antibacterial and anti-biofilm applications.

Previous studies have demonstrated the remarkable *in vitro* antibacterial activity of MnO_2. This study investigates the *in vivo* efficacy using a subcutaneous abscess model in MRSA-infected mice. All animal experiments were approved by the Institutional Animal Welfare and Ethics Review Committee of Wenzhou National Institute of Science and Technology (Wenzhou Institute of Biomaterials and Engineering Biology, WIUCAS24072202). The experimental procedure is illustrated in Fig. S6a (Supporting information). During the experiment, the wound temperature reached the therapeutic level (Fig. S6b in Supporting information). The body weight of the mice showed a steady increase (Fig. S6c in Supporting information). Representative wound images are displayed in Fig. 3a, demonstrating that wound healing in the MnO_2 group was superior to that in both the PBS and NIR groups. Interestingly, the wounds in the MnO_2 + NIR group exhibited a more complete healing status. The simulated wound area maps and quantitative analysis results (Fig. 3b and Fig. S6d in Supporting information) indicated that the final wound area ratios for the PBS group, NIR group, MnO_2 group, and MnO_2 + NIR group were 47.06%, 33.60%, 17.91%, and 4.89%, respectively. The bacterial plate counts of the wound tissues, as shown in Figs. S6e and f (Supporting information), indicated a reduction of 1.7 logCFU/mL (colony forming unit is abbreviated as CFU) in bacterial residue for the MnO_2 + NIR group. The therapeutic efficacy of MnO_2 *in vivo* was further evaluated through histopathological staining techniques, including hematoxylin and eosin (H&E), Masson, and Gram staining (Fig. 3c). H&E staining (the green arrow points to the scab of the wound and the inflammatory cells) revealed that the MnO_2 + NIR group exhibited more intact skin morphology and a lower percentage of inflammatory cells (18.61%) (Fig. S7a in Supporting information). The Masson trichrome staining method was employed to assess collagen deposition in the tissue. Red arrows indicate a significant number of fibrocytes that impede tissue healing. In contrast, blue arrows in the MnO_2 + NIR group highlight a large number of newly formed collagen fibers within the tissue, which is advantageous for wound healing (Fig. S7b in Supporting information). Additionally, Gram staining of the wound tissue revealed residual bacteria indicated by the yellow arrow (Fig. S7c in Supporting information). Macrophages play a crucial role in wound

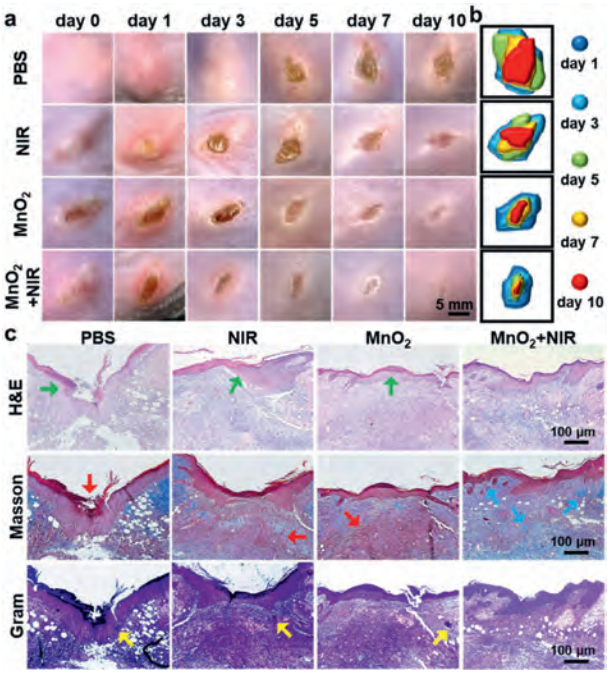


Fig. 3. Antibacterial effect of MnO_2 on the MRSA-infected subcutaneous abscesses mice model *in vivo*. (a) Representative photographs of subcutaneous abscesses on the MRSA-infected mice with different treatments. Scale bar: 5 mm. (b) Simulation diagram of subcutaneous abscess area. (c) From top to bottom, the histological graphs are representative of wound areas stained by H&E (green), Masson (blue and red) and Gram (yellow) in that order. Scale bar: 100 μm.

healing. This study conducted immunofluorescence analysis on the M1 marker protein inducible nitric oxide synthase (iNOS) (Figs. S8a and b in Supporting information) and the M2 marker protein Arginase 1 (Arg1) (Figs. S8c and d in Supporting information) in wound tissues. The expression of iNOS was most prominent in the PBS group, while the green fluorescence was weakest in the $MnO_2 + NIR$ group. Conversely, Arg1 exhibited the strongest fluorescence in the $MnO_2 + NIR$ group. The results of the immunofluorescence staining indicate that the expression of M2 macrophages was significantly higher in the $MnO_2 + NIR$ group, which effectively promoted the phased healing of the wound. Comparisons of iNOS and Arg1 expressions across the $MnO_2 + NIR$ treatment group revealed that this group exhibited the lowest levels of iNOS, indicating enhanced wound healing. Neovascularization is a critical indicator of wound healing, with higher expression of the CD31 marker associated with improved neovascularization. As shown in Figs. S8e and f (Supporting information), the $MnO_2 + NIR$ group demonstrated the highest CD31 expression. Overall, the combined photothermal and catalytic activity of manganese dioxide exhibited exceptional antibacterial and pro-inflammatory efficacy *in vivo*.

The effects of MnO_2 on major visceral tissues in mice were evaluated. As depicted by H&E staining in Fig. S9 (Supporting information), no significant differences in visceral tissues were observed between the groups, indicating the therapeutic safety of MnO_2 *in vivo*. Furthermore, as illustrated in Fig. S10 (Supporting information), the gray background denotes the normal threshold for each indicator (Figs. S10a–n). However, it is noteworthy that all indicators presented in Fig. S10 remain within normal limits. Specifically, Figs. S10a–d show that the liver function indicators alanine aminotransferase (ALT) and aspartate aminotransferase (AST), as well as the kidney function indicators blood urea nitrogen (BUN) and creatinine (CR), were all within normal ranges. Additionally, Figs. S10e–n demonstrate that all routine blood indicators, including monocyte (Mon), granulocyte (Gran), hemoglobin (HGB), lymphocyte (Lymph), red blood cell (RBC), white blood cell (WBC), platelet (PLT), mean red cell hemoglobin volume (MCH), basophil concentration value (BAS), and eosinophil concentration values (EOS), were also normal. Moreover, MnO_2 at various concentrations was found to be non-hemolytic, as shown in Fig. S10o. These results collectively demonstrate that MnO_2 possesses biosafety and biocompatibility.

Given the exceptional structural integrity, enzyme-like activity, photothermal effects, and biosafety, MnO_2 holds significant promise for future applications in biomedical and other research fields.

Declaration of competing interest

The authors declare that they have no known competing financial interests or personal relationships that could have appeared to influence the work reported in this paper.

CRediT authorship contribution statement

Jing Zhao: Writing – original draft, Methodology, Investigation. **Tian Huang:** Methodology, Investigation, Formal analysis. **Dongyang Zhang:** Methodology, Formal analysis, Data curation. **Jianliang Shen:** Supervision, Conceptualization. **Jintao Wang:** Writing – review & editing, Conceptualization.

Acknowledgments

This work is financially supported by the National Key Research and Development Program of China (No. 2022YFC2603900), the Zhejiang Provincial Natural Science Foundation for Distinguished Young Scholar (No. LR23C100001), the National Natural Science Foundation of China (No. 22067007), Jiangxi Provincial Natural Science Foundation, China (No. 20242BAB23024).

Supplementary materials

Supplementary material associated with this article can be found, in the online version, at doi:10.1016/j.cclet.2025.111199.

References

[1] T.G. Larsen, J.A. Samaniego Castruita, P. Worning, H. Westh, M.D. Bartels, Appl. Microbiol. Biotechnol. 108 (2024) 38924628.
[2] D.J. Morgan, R.P. Wenzel, G. Bearman, JAMA 318 (2017) 329–330.
[3] F. Hamilton, A. MacGowan, Nat. Microbiol. 4 (2019) 1604–1605.
[4] M. Qin, X. Zhang, H. Ding, et al., Adv. Mater. 36 (2024) e2402530.
[5] Z. Liu, F. Wang, J. Ren, X. Qu, et al., Biomaterials 208 (2019) 21–31.
[6] C. Gao, X. Qu, L. Fu, et al., Chem. Eng. J. 497 (2024) 154717.
[7] F.A. Al-Wrafy, A.A. Al-Gheethi, S.K. Ponnusamy, E.A. Noman, S.A. Fattah, Chemosphere 288 (2022) 132603.
[8] L. Chen, M. Peng, H. Li, et al., Adv. Mater. 36 (2023) 2306376.
[9] Y. Cheng, Y.D. Xia, Y.Q. Sun, Y. Wang, X.B. Yin, Adv. Mater. 36 (2023) 2308033.
[10] F. Cao, Y. Sang, C. Liu, et al., ACS Nano 16 (2022) 855–868.
[11] J. Lu, Y. Yang, Q. Xu, et al., Coord. Chem. Rev. 474 (2023) 214861.
[12] P. Zhao, H. Li, W. Bu, Angew. Chem., Int. Ed. 62 (2023) e202210415.
[13] N. Zhang, W. Ping, M. Suo, et al., Adv. Sci. 11 (2024) e2405575.
[14] L. Zhao, Y. Chen, Q. Wei, et al., Chem. Eng. J. 492 (2024) 152265.
[15] W. Wang, Y. Cui, X. Wei, et al., ACS Nano 18 (2024) 15845–15863.
[16] J. Huo, Q. Jia, H. Huang, et al., Chem. Soc. Rev. 50 (2021) 8762–8789.
[17] X. Qi, Y. Xiang, E. Cai, et al., Coord. Chem. Rev. 496 (2023) 215426.
[18] R. Ni, K.N. Opoku, X. Li, et al., Chin. Chem. Lett. 36 (2025) 110813.
[19] R. Zhang, Y. Zhou, S. Gao, J.L. Zhang, Chin. Chem. Lett. 37 (2026) 110829.
[20] G. Yang, J. Ji, Z. Liu, WIREs Nanomed. Nanobiotechnol. 13 (2021) e1720.
[21] Y. Meng, R. Han, Q. Tian, Y. Chen, L. Zhang, Adv. Healthc. Mater. 13 (2024) 2304141.
[22] H.-Y. Xia, B.-Y. Li, Y. Zhao, et al., Coord. Chem. Rev. 464 (2022) 214540.
[23] L.S. Lin, J. Song, L. Song, et al., Angew. Chem. Int. Ed. 57 (2018) 4902–4906.
[24] F. Wang, Q. Wu, G. Jia, et al., Adv. Sci. 10 (2023) e2303911.
[25] L. Xie, X. Zhang, X. Wang, et al., Chin. Chem. Lett. 36 (2025) 110848.
[26] Y. Zheng, K. Fu, Z. Yu, et al., J. Mater. Chem. A: Mater. 10 (2022) 14171–14186.
[27] J. Ma, M. Yuan, Z. Yang, et al., J. Am. Chem. Soc. 146 (2024) 22348–22359.
[28] X.L. Hao, J.Z. Zhao, Y.H. Song, et al., J. Nano Res. 53 (2018) 1–6.

[29] J. Jia, P. Zhang, L. Chen, Appl. Catal. B 189 (2016) 210–218.
[30] F. Wang, H. Dai, J. Deng, et al., Environ. Sci. Technol. 46 (2012) 4034–4041.
[31] L. Cheng, F. Wu, H. Bao, et al., Small 17 (2021) e2104083.
[32] Z. Yang, L. Wang, X. Zhang, et al., ACS Nano 18 (2024) 24469–24483.
[33] Z. Lin, J. Yuan, L. Niu, et al., Coord. Chem. Rev. 520 (2024) 216166.
[34] L. Fang, J. Dai, X. Wang, et al., Small 21 (2025) e2409196.
[35] G.A. Smith, T.H. Lin, A.E. Sheehan, et al., Neuron 103 (2019) 52–65 e6.
[36] L. Wu, Y. Meng, X. Zheng, et al., Chin. Chem. Lett. 36 (2025) 110808.